A Calibration Technique for Simultaneous Estimation of Actual Sensing Matrix Coefficients on Modulated Wideband Converters

Zolboo Byambadorj, *Graduate Student Member, IEEE*, Koji Asami, *Member, IEEE*, Takahiro J. Yamaguchi, *Member, IEEE*, Akio Higo, *Member, IEEE*, Masahiro Fujita, *Member, IEEE*, and Tetsuya Iizuka, *Senior Member, IEEE*

***Abstract*— The Modulated Wideband Converter (MWC) is one of the promising sub-Nyquist sampling architectures for sparse wideband signal sensing applications. Its frequency support detection and the reconstruction ability is well-defined through compressed sensing theory. However, the reconstruction performance of the MWC is strictly limited by the non-ideal components in practical implementations. Previous calibration methods exploit sequential single-tone signals to estimate the actual transfer function of the MWC, which is fairly time-consuming. We propose a new calibration method that estimates the actual sensing matrix coefficients of the MWC only with a single measurement based on a pilot multi-tone signal. The feasibility of the proposed calibration method is demonstrated in terms of normalized mean square error (NMSE) and image rejection ratio (IRR) of the reconstructed original signal.**

***Index Terms*— Modulated wideband converter, compressed sensing, sparse wideband signal spectrum sensing, calibration method, practical implementation.**

I. Introduction

MULTIBAND signal sensing has been successfully applied to cognitive radios and spectrum analyzers [1]–[3]. However, the target bandwidth becomes significantly wider to drive a constantly increasing demand of data-rate in wireless communications. Unfortunately, a sampling speed of current commercial analog-to-digital converters are often insufficient to capture such wideband signal based on Shannon-Nyquist theorem [4], [5] that states that the sampling speed must be at least twice higher than the bandwidth of the signal.

Manuscript received April 29, 2020; revised July 13, 2020; accepted August 6, 2020. Date of publication September 1, 2020; date of current version December 1, 2020. This article was recommended by Associate Editor H. Zhang. *(Corresponding author: Zolboo Byambadorj.)*

Zolboo Byambadorj is with the Department of Electrical Engineering and Information Systems, The University of Tokyo, Tokyo 113-0032, Japan (e-mail: zolboo@silicon.u-tokyo.ac.jp).

Koji Asami is with Advantest Laboratories Ltd., Miyagi 989-3124, Japan (e-mail: koji.asami@advantest.com).

Takahiro J. Yamaguchi, Akio Higo, Masahiro Fujita, and Tetsuya Iizuka are with the Systems Design Laboratory, School of Engineering, The University of Tokyo, Tokyo 113-0032, Japan (e-mail: takahiro.j.yamaguchi@vdec.u-tokyo.ac.jp; higo@if.t.u-tokyo.ac.jp; fujita@ee.t.u-tokyo.ac.jp; iizuka@vdec.u-tokyo.ac.jp).

Color versions of one or more of the figures in this article are available online at https://ieeexplore.ieee.org.

Digital Object Identifier 10.1109/TCSI.2020.3017521

Mitigating the hardware overhead of a multiband signal sensing, several hardware-efficient sub-Nyquist sampling architectures are proposed over the past decades. Among them, the modulated wideband converter (MWC), firstly appeared in [6], shows interesting architecture based on the compressed sensing theory to effectively capture sparse multiband signals. Although the recovery process and the reconstruction procedure for the sensed multiband sparse signal is ideally well-defined by sensing matrix of the compressed sensing in mathematical frameworks, the existing implementations including quadrature analog-to-information converter (QAIC), time-segmented QAIC (TS-QAIC) and random triggering based modulated wideband compressive sampling (RT-MWCS) in [7]–[20] face several practical issues related to the non-ideality of the analog components including mixer, low-pass filter (LPF) and analog-to-digital converter (ADC) that cause uncertain deviation on the sensing matrix from its ideal value. Without calibrating the sensing matrix, realization of the reconstruction and the recovery of support becomes infeasible. The previous works [7]–[10], [21]–[23] exploit the estimation method for actual sensing matrix based on a set of sequential measurements of single-tones with known frequencies. This iterative method is extremely time-consuming and the digital processing of the calibration turns into computationally complex due to the large number of calibration signals for real-time applications. In addition, the accuracy of the calibration may be deteriorated by the measurement-to-measurement timing mismatch.

In this paper, we propose a novel calibration method for simultaneous estimation of all the components of the actual sensing matrix based on a single measurement with a non-sparse pilot signal. Not only the number of measurement is reduced in the proposed method, but also the measurement-to-measurement timing fluctuations in the calibrated sensing matrix are fundamentally suppressed. The performance of the proposed calibration method is demonstrated in terms of normalized mean square error (NMSE) and image rejection ratio (IRR) for the reconstruction of the original time-domain waveform. To the best of our knowledge, previous applications of the MWC are all intended to be used for detecting power on specific frequencies without reconstructing the original time-domain waveform itself as in [8], [9], [21], [24]. In

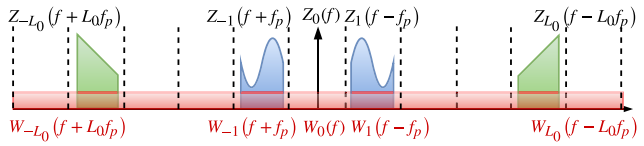

Fig. 1. Input sparse signal spectrum model.

this research work, we will discover the high performance possibility of the reconstruction process for the original time-domain waveform based on the MWC.

The remainder of this paper is organized as follows. Section II provides some preliminary background of the wideband sparse signal and the MWC system. Section III presents a conventional calibration method for the MWC, whereas the proposed calibration method is discussed in Section IV. Section V demonsrates the implementation setup and the achieved performance is discussed. Finally, this paper is concluded in Section VI.

II. Preliminaries

A. Wideband Sparse Signals

Frequency-domain representation is useful to define a wideband sparse signal rather than its time-domain definition [25]. The frequency-domain representation of a multiband signal can be modeled as

$$X(f) = \sum_{l=-L_0}^{L_0} Z_l(f - lf_p), \tag{1}$$

where $Z_l(f)$ is a separate spectrum slice placed at baseband and carrier frequencies are assumed to be aligned with integer multiples of f_p here. As shown in Fig. 1, the frequency-shifted version of $Z_l(f)$ is sparsely placed in the frequency domain. The number of slots within the band of interest is counted as L_0 in (1).

If the signal is spectrally sparse, most of $Z_l(f)$ are zero. So (1) is rewritten as

$$X(f) = \sum_{l \in \mathbf{S}} Z_l(f - lf_p), \tag{2}$$

where $\mathbf{S}$ is a support of $X(f)$, which is a set of N indices that correspond to carrier frequencies (including conjugate frequencies) of active bands. As the signal is spectrally sparse, $N \ll L$. Furthermore, another important assumption is that each active band signal has a bandwidth B which is narrower than f_p so that any active band signals do not overlap with each other.

B. Modulated Wideband Converter (MWC)

Based on the MWC settings defined in [6], a basic MWC system is illustrated in Fig. 2 [25]. The main architecture of the MWC is divided into three parts to demonstrate its input and output dependence step by step. Part 1 includes a mixer that mixes the input signal with a mixing function $p_i(t)$ and an LPF that retains baseband part of the mixed signal. Part 2 indicates the conversion of the analog signal to the digital signal, while

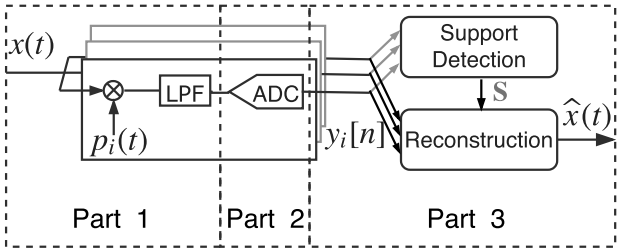

Fig. 2. Basic MWC system block diagram.

TABLE I
MWC Design Parameters

Design Parameters	Notation
Periodic Sign Function (PSF) frequency	f_p
Number of active bands	N
Number of slots in band of interest	L
Band of interest	$W = Lf_p$
Bandwidth of active band	B
Number of symbols in PSF	M
Number of channels	m
Carrier Frequencies	f_i
Number of digital channels in a single channel	q
Sampling rate of ADC	$f_s = qf_p$
Number of bits on ADC	NOB

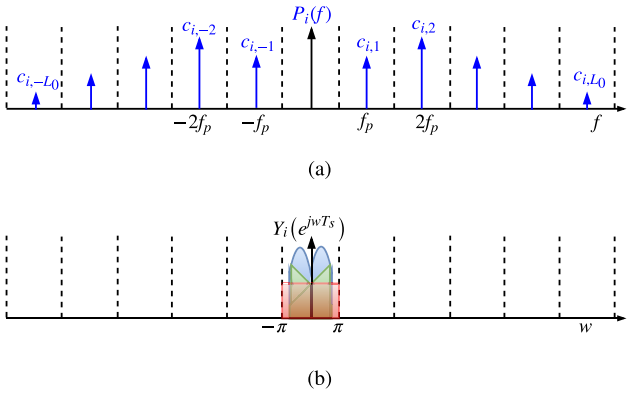

Fig. 3. (a) Fourier Series of the i-th PSF, (b) DTFT of the i-th sampled signal of the basic MWC.

Part 3 includes digital processing such as digital modulation, support detection and reconstruction of the original signal. The design parameter notations are summarized in Table I.

A periodic sign function (PSF) $p_i(t)$ is a periodically constant sequence with M length that switches the level between -1 and $+1$ for $T_p = 1/f_p$ interval. Formally,

$$p_i(t) = \alpha_{i,j}, \quad j\frac{T_p}{M} \le t \le (j+1)\frac{T_p}{M}, \quad 0 \le j \le M-1 \tag{3}$$

with a random $\alpha_{i,j} \in \{+1, -1\}$ [6]. A frequency-domain illustration of a PSF $p_i(t)$ that is decomposed into Fourier series coefficients $c_{i,l}$ located at lf_p is shown in Fig. 3(a). These components downconvert corresponding bands or spectrum slices of the input signal with individual amplitudes as in Fig. 3(b), where the i-th digital output signal $y_i[n]$ through

Fourier transform can be expressed as

$$Y_i(e^{jwT_s}) = \sum_{l=-L_0}^{L_0} c_{i,-l} Z_l(f). \tag{4}$$

If (4) is written as a vector signal $\mathbf{Y} = [Y_1(e^{jwT_s}), Y_2(e^{jwT_s}), \ldots Y_m(e^{jwT_s})]^T$ in matrix form where the superscript T represents transpose, the generalized form is given by

$$\mathbf{Y} = \mathbf{AZ}, \tag{5}$$

where $\mathbf{Z}$ points out separate spectrum slices of the input discrete-time signal and $\mathbf{A}$ is a sensing matrix that is defined only by Fourier series coefficients of all PSF signals as

$$[\mathbf{A}]_{i,j} = c_{i,j}, \quad i \in [1, m], \quad j \in [-L_0, L_0]. \tag{6}$$

The parameter q in Table I enables design flexibility between the number of analog channels and the complexity of digital signal processing by increasing the sampling rate of the ADC in each channel to capture more frequency bands into digital domain [25]. Although the detailed explanation is omitted in this paper, in the case of a so-called advanced MWC, q (> 1) digital channels are effectively extracted from a single analog channel [25].

Once we have a digital vector signal, we have to recover support frequencies of active bands in the input wideband sparse signal using Greedy algorithms such as matching pursuit (MP), orthogonal matching pursuit (OMP), etc [26]. Recovered support frequency indicates nonzero signal indices of $\mathbf{Z} = [Z_{-L_0}(f), \ldots, Z_0(f), \ldots, Z_{L_0}(f)]^T$. These nonzero signals can be reconstructed using least-squares through the multiplication of the pseudo-inverse matrix as follows:

$$\hat{\mathbf{Z}}_\mathbf{S} = \mathbf{A}_\mathbf{S}^\dagger \mathbf{Y} \tag{7}$$

Here, subscript $\mathbf{S}$ denotes a set of row indices where $\mathbf{Z}$ takes nonzero values. In more detail, $\mathbf{A}_\mathbf{S}^\dagger = (\mathbf{A}_\mathbf{S}^\mathbf{H}\mathbf{A}_\mathbf{S})^{-1}\mathbf{A}_\mathbf{S}^\mathbf{H}$, where $\mathbf{A_S}$ denotes a submatrix of $\mathbf{A}$ formed from a column set $\mathbf{S}$ and $\mathbf{A}^\mathbf{H}$ indicates Hermitian matrix that is equal to its own conjugate transpose.

III. Conventional Calibration Method for the MWC

In this section, two different conventional calibration methods based on the single-tone training signal are introduced. The single-tone training signal can be written as

$$\tilde{x} = \cos(2\pi f_t t), \tag{8}$$

where f_t is the frequency of the training signal. Depending on the choice of the f_t, two different calibration methods are introduced by the literatures [9], [22].

A. Case $f_t = kf_p, k \in \mathbb{Z}$

The literature [22] proposed the calibration method based on the single-tone training signal. The frequency of the training signal is iteratively adjusted with $f = 2\pi k f_p$ where $1 \le k \le L_0$. The training signal is defined by

$$\tilde{x}(t) = \cos(2\pi (kf_p)t). \tag{9}$$

After the MWC processes, the sampled signal in the i-th channel is written as

$$\tilde{y}_i[n] = \frac{1}{2}(c_{i,k} + c_{i,-k}). \tag{10}$$

Considering the property $c_{i,k} = c_{i,-k}^*$, the following equation is obtained

$$\mathrm{Re}\{c_{i,-k}\} = \tilde{y}_i[n]. \tag{11}$$

Applying similar discussion to $\sin(2\pi(kf_p)t)$ where $1 \le k \le L_0$ then the sampled signal in the i-th channel is

$$\tilde{y}_i[n] = \frac{j}{2}(c_{i,k} - c_{i,-k}), \tag{12}$$

which leads to

$$\mathrm{Im}\{c_{i,-k}\} = \tilde{y}_i[n]. \tag{13}$$

This calibration procedure starts with cosine wave by setting the input frequency to f_p. Then, the real component of $c_{i,-k}$ is directly obtained from the output of the ADC as in (11). After that, the input signal is changed into sine wave with the same frequency. In the same manner, the imaginary component of $c_{i,-k}$ is directly obtained from the output of the ADC as in (13). From these two measurements, $c_{i,-k}$ is obtained. By iteratively changing the frequency and repeating the procedure, the exact elements in the actual matrix $\mathbf{A}$ can be calculated [22].

This approach needs $2L_0$ measurements for the calibration of actual sensing matrix that may includes measurement-to-measurement timing and gain mismatches due to the uncertainty in the ADC sampling timing, channel-to-channel timing skew of the signal source, etc.

B. Case $f_t \neq kf_p, k \in \mathbb{Z}$

The literature [9] proposed a calibration method based on the single-tone signal as given by

$$\tilde{x} = \sin(2\pi(kf_p + f_0)t), k \in [0, 1, \ldots, L_0]. \tag{14}$$

Here, the bias frequency f_0 is set within the range of $0 < f_0 < f_p/2$. After the MWC processes, the sampled signal in the i-th channel is written as

$$\tilde{y}_i[n] = c_{i,k} \sin(2\pi f_0 n T_s). \tag{15}$$

Due to the impact of some added noise and nonlinear effects of the mixer, the $\tilde{y}_i[n]$ contains additional harmonics at DC, bf_p and bf_0 for $b \in \mathbb{N}$. To extract the $c_{i,k}$ term, first they removed DC component by subtracting the mean value of the signal. Then they estimated the actual frequency $\tilde{f_0}$ based on Welch's spectrum estimation [27]. Finally, they applied a least square method to estimate the $c_{i,k}$ based on

$$\underset{c_{i,k}}{\mathrm{argmin}} \|\tilde{y}_i[n] - c_{i,k} \sin(2\pi \tilde{f_0} n T_s)\|^2. \tag{16}$$

After performing $L_0 + 1$ iterations of the above calibration procedure, the sensing matrix is obtained [9]. Using $f_t \neq kf_p, k \in \mathbb{Z}$, the complex number $c_{i,k}$ is obtained from one measurement in this method while the previous method in Sect. III-A requires two. Thus this approach reduces the total number of measurement to L_0.

IV. Proposed Calibration Technique

In this section, the proposed calibration technique is explained in comparison to the conventional calibration method discussed in Sect. III. First, we define a pilot signal that is necessary for the proposed calibration technique. Afterwards, the estimation method of the actual sensing matrix based on the pilot signal is proposed.

A. Pilot Signal Generation

Although the MWC is designed for wideband sparse signal, we exploit a dedicated non-sparse signal for this calibration technique as shown in Fig. 4(a). The sparse signal in this paper is defined as the signal that covers a limited number of bands or spectrum slices within the band of interest. Thus the pilot signal is recognized as a non-sparse signal, because the tones spread all over the bands. The pilot signal for the calibration is composed of multiple tones as given by

$$\tilde{x}(t) = \sum_{l=1}^{L_0} \cos(2\pi (l f_p + f_l)t + \phi_l), \tag{17}$$

where ϕ_l is an initial phase and f_l is a pilot single-tone frequency that lies within $f_p/2$. The set of the phases is important to limit the crest factor in order to maximize the dynamic range within a limited full-scale range of the ADC. For this purpose, the Newman phases are used in this paper to present low crest factor. According to [28], the Newman phases can be given by

$$\phi_l = \frac{\pi (l-1)^2}{L_0}. \tag{18}$$

In more detail on the frequency set, f_l can be linearly spaced for straightforward understanding as

$$f_l = f_0 + l\Delta f. \tag{19}$$

Here, f_0 is an offset frequency for all tones, Δf is a constant distance between two tones. In the frequency-domain, (17) is rewritten as

$$\tilde{X}(f) = \sum_{l=-L_0}^{L_0} \tilde{Z}_l(f - l f_p) = \sum_{l=-L_0}^{L_0} e^{j\phi_l} \delta(f - l f_p - f_l), \tag{20}$$

where each $\tilde{Z}_l(f)$ spectrum slice of the input signal contains single-tone at $l f_p + f_l$ as illustrated in Fig. 4(a).

B. MWC With Pilot Signal

In order to identify the actual transfer function deviated due to hardware-related non-idealities, the pilot signal explained above is used as the input to the MWC. The discrete-time Fourier transform of the i-th output (4) of the ADC is given by

$$\tilde{Y}_i(e^{j\omega T_s}) = \sum_{l=-L_0}^{L_0} \tilde{c}_{i,-l} \delta(f - f_l). \tag{21}$$

Here, $\tilde{c}_{i,-l}$ is a Fourier series coefficients of the *actual* PSF, which is not equal to the *ideal* $c_{i,-l}$. Each single tone at f_l from each spectrum slice $\tilde{Z}_l(f)$ of the pilot signal in Fig. 4(a) is mixed with the corresponding *actual* coefficient $\tilde{c}_{i,-l}$ of the PSF in Fig. 4(b) and the downconverted part of the mixer output is illustrated in Fig. 4(c). The main advantage of the pilot signal can be seen in (21); the downconverted components are disjoint in the frequency-domain. Then (5) is rewritten as

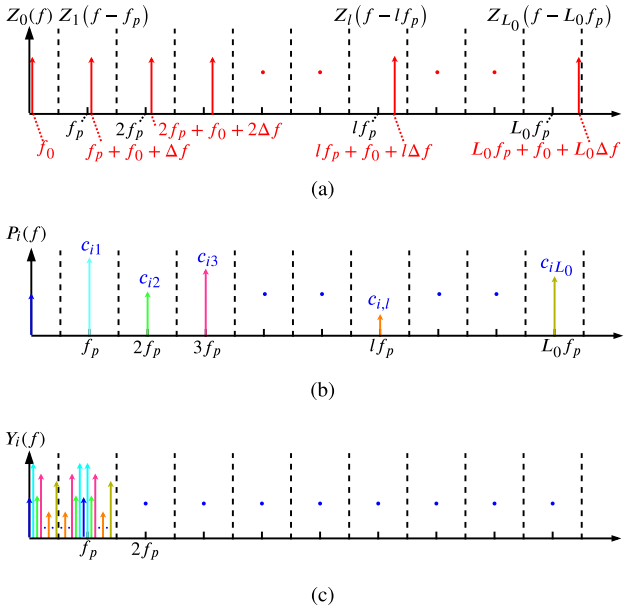

Fig. 4. (a) Spectrum of the pilot signal, (b) Fourier series of the i-th PSF and (c) spectrum of the mixer output.

$$\tilde{\mathbf{Y}} = \tilde{\mathbf{A}}\tilde{\mathbf{Z}}, \tag{22}$$

where $\tilde{\mathbf{Y}} = [\tilde{Y}_1(e^{j\omega T_s}), \tilde{Y}_2(e^{j\omega T_s}), \ldots \tilde{Y}_m(e^{j\omega T_s})]^T$, $\tilde{\mathbf{Z}} = [\tilde{Z}_{-L_0}(f), \ldots, \tilde{Z}_{-1}(f), \tilde{Z}_0(f), \tilde{Z}_1(f), \ldots \tilde{Z}_{L_0}(f)]^T$ and $\tilde{\mathbf{A}}_{i,j} = \tilde{c}_{i,j}$. In other words, $\tilde{Z}_l(f)$ contains only one nonzero component in the frequency domain. Based on this advantage, (22) can be rewritten as

$$\tilde{Y}_i(e^{j2\pi f_l T_s}) = [\tilde{\mathbf{A}}]_{i,l} \tilde{Z}_l(f_l), \tag{23}$$

so that each component $\tilde{Y}_i$ of $\tilde{\mathbf{Y}}$ is independent of other components of $\tilde{\mathbf{Z}}$ in (22).

C. Calibration of the Actual Sensing Matrix

According to (23) and its disjoint feature of the mixer output signal in the frequency-domain, the actual coefficients of the sensing matrix can be independently calculated as

$$\tilde{c}_{i,l} = \frac{\tilde{Y}_i(e^{j2\pi (f_l) T_s})}{\tilde{Z}_l(f_l)} \quad \text{for all} \quad l \in [-L_0, L_0],\ i \in [1, m]. \tag{24}$$

The pilot signal is non-sparse as it covers many bands within the frequency of interest, thus the MWC does not have a capability to reconstruct it. However, based on (24) the coefficients of the sensing matrix are extracted without reconstructing the original pilot signal. The calculation of the whole sensing matrix coefficients needs only a single

measurement with the pilot signal in the proposed calibration method.

The advantages of the proposed calibration technique are summarized as follows:

- The ideal reconstruction of the MWC in [6] assumes that there is no time difference between the PSF and the ADC clock. However, the time difference is introduced by a non-zero wiring delay in the practical implementation. This time difference can be taken into account as a linear phase shift in the sensing matrix as pointed out by [7], [21], [29]. In the proposed technique, the time difference between PSF and ADC clock is automatically included in the *actual* $\tilde{c}_{i,l}$ in (24). For example, if a time delay t_i exists between i-th PSF and the ADC clock (explained later in Fig. 7(b)), then it introduces additional $e^{j2\pi l f_p t_i}$ phase shift on l-th component $c_{i,l}$ of the PSF. That phase shift will be directly measured by l-th tone of the pilot signal at $lf_p + f_l$ frequency then the mixer downconverts the phase-shifted component into f_l frequency. Therefore the phase shift information appears in $\tilde{Y}_i(e^{j2\pi f_l T_s})$ so that $\tilde{c}_{i,l}$ obtains the $e^{j2\pi l f_p t_i}$ phase shift through (24).
- The conventional method does not have a capability to estimate the accurate *initial phase* of the single-tone signal. The reason is that the *initial phase* of the single-tone signal is shifted by the phase characteristics of the transfer function as well as by a measurement-to-measurement timing fluctuation. This timing fluctuation in the single-tone sequential measurement results in unexpected phase rotations on each sensing matrix coefficient, which in consequence leads to a reconstruction failure. However, in the proposed calibration method, all the coefficients in the sensing matrix is obtained from the single measurement so that the phase rotations of all the coefficients are identical. Even if the sampling timing in the actual measurement is shifted from that in the calibration, it just introduces some time shift in the time-domain waveform, which does not distort the waveform shape. The *initial phase* is also necessary to find the starting point of the signal so that the timing mismatch can be compensated in the multi-channel MWC. The relative phases between tones in the pilot signal are defined by the Newman phases as introduced in Sect. IV. Using this relation the *initial phase* of the input signal can be calculated precisely.
- Similar to the initial phase estimation, the gain mismatch of the multi-channel is also detectable based on the pilot signal. These gain and timing mismatches are necessary to be compensated in the multi-channel MWC to avoid a reconstruction failure.

D. The Reconstruction Performance Based on NMSE and IRR

The quantification of the reconstruction performance of the MWC is necessary to demonstrate the effectiveness of the calibration method. For that reason, the normalized mean square error (NMSE) of the time-domain reconstructed signal $\hat{x}(t)$ with respect to the original input signal $x(t)$ is defined as follows:

$$\mathrm{NMSE_{dB}} = 10\log_{10}\int_{-\infty}^{\infty}\frac{\|x(t)-\hat{x}(t)\|^2}{\|x(t)\|^2}dt. \tag{25}$$

Here, the mean square error (MSE) part in the numerator $\frac{1}{T}\int_0^T \|x(t)-\hat{x}(t)\|^2$ is normalized by the average signal power $\frac{1}{T}\int_0^T \|x(t)\|^2$ in the denominator. As the reconstructed time-domain waveform $\hat{x}(t)$ approaches closer to the original input waveform $x(t)$, the MSE part reaches to 0 then NMSE in decibel goes to minus direction.

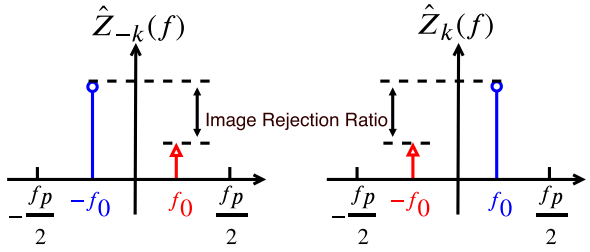

Fig. 5. The reconstructed original single-tone and its unwanted image are highlighted as blue circles and red triangles in the frequency-domain, respectively.

The alternative way to quantify the reconstruction performance is an image rejection ratio (IRR). The actual sensing matrix $\tilde{\mathbf{A}}$ is no longer an inverse of the ideal $\mathbf{A}_\mathbf{S}^\dagger$ that results in $\mathbf{A}_\mathbf{S}^\dagger\tilde{\mathbf{A}}\mathbf{Z} \neq \mathbf{Z}_\mathbf{S}$. In more detail, the image is introduced when the single-tone is injected. Supposing that the input single-tone is given by

$$x(t) = \cos(2\pi(kf_p + f_0)t), \tag{26}$$

where $f_0 < f_p/2$, its frequency-domain components are defined as

$$X(f) = \frac{1}{2}(\delta(f - kf_p - f_0) + \delta(f + kf_p + f_0)) \tag{27}$$

such that $\mathbf{S} = \{-k, k\}$. Then the nonzero spectrum slices of the input signal as in (2) is given by

$$Z_k(f) = \frac{1}{2}\delta(f - f_0) \tag{28}$$

$$Z_{-k}(f) = \frac{1}{2}\delta(f + f_0) \tag{29}$$

Recalling (4), the i-th digital output of the ADC in the MWC is expressed by

$$Y_i(e^{j\omega T_s}) = \tilde{c}_{i,-k}Z_k(f) + \tilde{c}_{i,k}Z_{-k}(f) \tag{30}$$

$$= \frac{1}{2}(\tilde{c}_{i,-k}\delta(f - f_0) + \tilde{c}_{i,k}\delta(f + f_0)). \tag{31}$$

After the reconstruction as in (7) with $m = 2$ case, the reconstructed spectrum slices are given by

$$\hat{Z}_k(f) = \frac{1}{2}[\mathbf{A}_\mathbf{S}^\dagger]_{1,1}(\tilde{c}_{1,-k}\delta(f - f_0) + \tilde{c}_{1,k}\delta(f + f_0)) + \frac{1}{2}[\mathbf{A}_\mathbf{S}^\dagger]_{1,2}(\tilde{c}_{2,-k}\delta(f - f_0) + \tilde{c}_{2,k}\delta(f + f_0)), \tag{32}$$

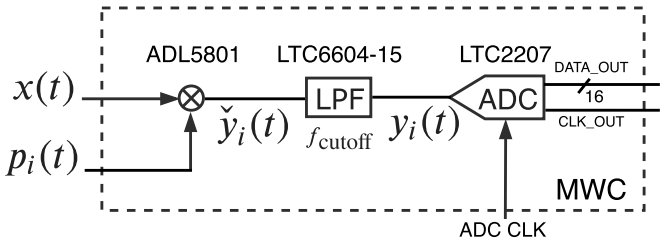

Fig. 6. The MWC implementation setup.

which leads to

$$\hat{Z}_k(f) = \frac{1}{2}([\mathbf{A}_\mathbf{S}^\dagger]_{1,1}\tilde{c}_{1,-k} + [\mathbf{A}_\mathbf{S}^\dagger]_{1,2}\tilde{c}_{2,-k})\delta(f - f_0) + \frac{1}{2}([\mathbf{A}_\mathbf{S}^\dagger]_{1,1}\tilde{c}_{1,k} + [\mathbf{A}_\mathbf{S}^\dagger]_{1,2}\tilde{c}_{2,k})\delta(f + f_0). \tag{33}$$

Assuming the ideal case where

$$([\mathbf{A}_\mathbf{S}^\dagger]_{1,1}c_{1,-k} + [\mathbf{A}_\mathbf{S}^\dagger]_{1,2}c_{2,-k}) = 1$$
$$([\mathbf{A}_\mathbf{S}^\dagger]_{1,1}c_{1,k} + [\mathbf{A}_\mathbf{S}^\dagger]_{1,2}c_{2,k}) = 0, \tag{34}$$

the reconstructed spectrum results in

$$\hat{Z}_k(f) = \frac{1}{2}\delta(f - f_0). \tag{35}$$

Here the image component $\delta(f + f_0)$ is completely rejected. However, considering $\tilde{c}_{i,l} \neq c_{i,l}$ in the practical case, (34) is no longer true where

$$[\mathbf{A}_\mathbf{S}^\dagger]_{1,1}\tilde{c}_{1,-k} + [\mathbf{A}_\mathbf{S}^\dagger]_{1,2}\tilde{c}_{2,-k} \neq 1 \tag{36}$$
$$[\mathbf{A}_\mathbf{S}^\dagger]_{1,1}\tilde{c}_{1,k} + [\mathbf{A}_\mathbf{S}^\dagger]_{1,2}\tilde{c}_{2,k} \neq 0 \tag{37}$$

Consequently, $\delta(f + f_0)$ is not completely suppressed and it appears on the reconstructed $\hat{Z}_k(f)$ spectrum slice as an image of the original component $\delta(f - f_0)$ as illustrated in Fig. 5. The image rejection ratio (IRR) in Fig. 5 is defined by

$$\text{IRR}_{\text{dB}} = 10\log_{10}\frac{\|Z_k(f_0)\|^2}{\|Z_k(-f_0)\|^2}, \tag{38}$$

which is a power ratio of the original and the image components. In the case of $m = 2$, the IRR is given by

$$\text{IRR}_{\text{dB}} = 10\log_{10}\frac{\left\|[\mathbf{A}_\mathbf{S}^\dagger]_{1,1}\tilde{c}_{1,-k} + [\mathbf{A}_\mathbf{S}^\dagger]_{1,2}\tilde{c}_{2,-k}\right\|^2}{\left\|[\mathbf{A}_\mathbf{S}^\dagger]_{1,1}\tilde{c}_{1,k} + [\mathbf{A}_\mathbf{S}^\dagger]_{1,2}\tilde{c}_{2,k}\right\|^2}. \tag{39}$$

The deviated sensing matrix deteriorates the reconstruction by introducing images of the original signal. To quantify such distortion, the IRR measures the ratio of the image signal power and original signal power regardless of any other components in the frequency domain. The IRR differs from the NMSE by measuring the reconstruction performance in the frequency domain while the NMSE is calculated in the time domain.

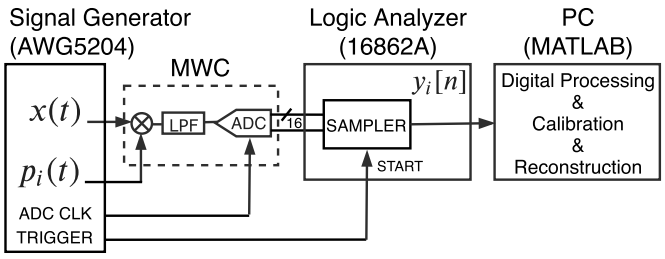

(a)

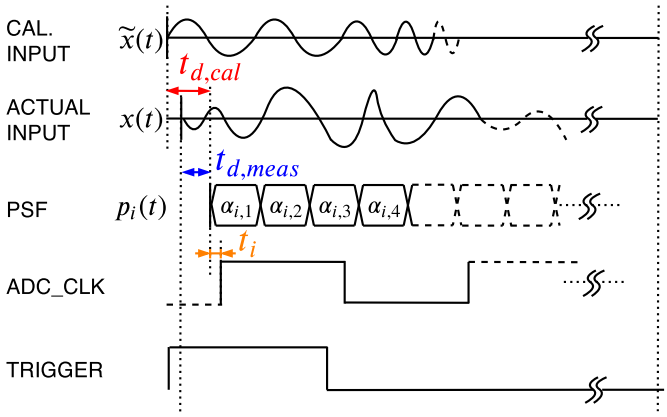

(b)

Fig. 7. (a) The measurement setup and (b) its timing diagram. t_i is the time difference between the PSF and the ADC clock in i-th channel. $t_{d,cal}$ and $t_{d,meas}$ are the time differences of the calibration input and the actual measurement input relative to the PSF, respectively.

V. Implementation Setup and Measurement Results

In this section, the proposed calibration method explained in Sect. IV is deployed to a practical implementation setup of the MWC.

A. Implementation Setups and MWC Design Parameters

The MWC implementation setup is depicted in Fig. 6 and the measurement setup is shown in Fig. 7(a). The timing diagram of the measurement setup is illustrated in Fig. 7(b). t_i is a time difference between the PSF and the ADC clock in i-th channel. $t_{d,cal}$ is a time difference between the start of the calibration signal and the PSF and $t_{d,meas}$ is a time difference between the start of the actual input signal and the PSF. These unwanted time differences are unavoidable due to the actual measurement setup such as cable delays and timing skews of the measurement equipments. We are providing a single pulse as the trigger signal that controls the logic analyzer to start the measurement. First of all, t_i is one of the important non-ideal factors that introduces phase deviation on the actual sensing matrix and how it is compensated in the calibration is explained in Sect. IV-C. The $t_{d,cal}$ in the proposed calibration introduces just a linear phase shift on the sensing matrix. Even though the $t_{d,cal}$ is not guaranteed to be the same as $t_{d,meas}$ in the actual measurement procedure, such delay has no effect on the sensing matrix but results in a simple time

TABLE II
THE DESIGN PARAMETERS OF MWC IMPLEMENTATION

Implementation Design Parameters	Notation	Value
Periodic Sign Function (PSF) frequency	f_p	1 MHz
Number of active bands	N	2
Number of slots in band of interest	L	160
Band of interest	W	160 MHz
Bandwidth of active band	B	1 MHz
Number of symbols in PSF	M	500
Number of channels	m	4
Carrier Frequencies	f_i	$(11-90)$ MHz
Number of digital channels	q	17
Sampling rate of ADC	f_s	100 MHz
Number of bits on ADC	NOB	16 bits

shift in the reconstructed time-domain waveform. On the other hand, the $t_{d,cal}$ in the conventional method throughout all the sequential measurements may be fluctuated. These fluctuations result in different phase shift in each coefficient that introduces distortion on the reconstructed time-domain waveform, not just a simple time shift.

The design parameters of the MWC are summarized in Table II. Note that N, L, M parameters count conjugate frequency components as well.

1) Analog Mixer: One of the most crucial components in the MWC system is an analog mixer that must have a capability to accept wideband local oscillator (LO) input signal. The reason is that the nature of the MWC system needs to mix the radio frequency (RF) input signal with the PSF that occupies wide bandwidth. However, most of the typical analog mixer is designed to be used with single-tone LO signal. For this realization, the high third-order intercept point (IP3) active mixer ADL5801 [30] is used in this paper. Its frequency range is sufficiently large from 10 MHz to 6 GHz.

2) Low-Pass Filter (LPF): A fully differential 15 MHz 4-th order low-pass filter LTC6604-15 [31] is used as the LPF.

3) ADC: A 16-bits, 105 MS/s ADC, LTC2207 [32] is selected for the high-precision measurement. The sampling speed is set to 100 MHz in this measurement as shown in Table II. The parallel digital output is read by the logic analyzer to export the measured data. Afterward, the digital domain processing and the reconstruction is carried out in MATLAB environment.

4) Emulation of Multi-Channel MWC: We emulate the multi-channel MWC using a single-channel MWC by taking multiple measurements with different PSFs.

The test signals including the pilot signal, the PSF and the ADC clock were delivered by an arbitrary waveform generator (AWG, Tektronix AWG5204) that supports 4 differential outputs at 5 GHz sampling rate. The waveform files were generated in MATLAB environment in advance. The synchronization signal and 10 MHz clock signal are also distributed by the AWG to the logic analyzer (Keysight 16862A) for synchronization purpose.

B. Calibration Procedure

As previously discussed in Sect. IV, the calibration of the actual sensing matrix is carried out using the non-sparse pilot signal. To generate the multi-tones, we may need an AWG equipment rather than a simple sinewave generator. For the experimental comparison, we implemented the conventional calibration method explained in Sect. III-B as well as the proposed method. The maximum amplitude of the multi-tone pilot signal in the proposed method is set equal to the amplitude of the single-tones in the conventional method in the following experiment.

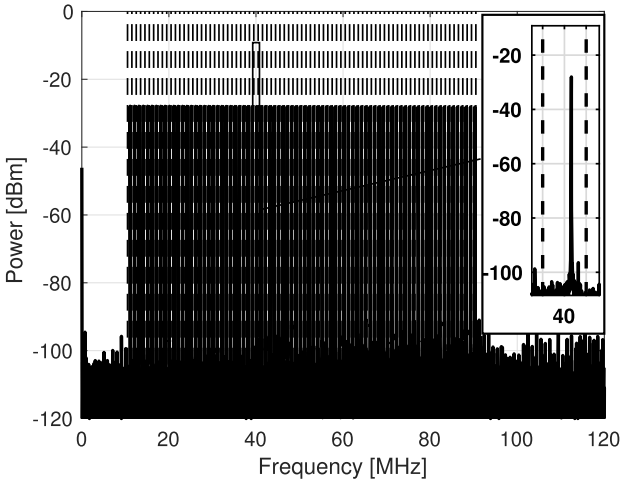

Fig. 8. Frequency-domain spectrum of the measured pilot signal. In the zoomed-in view, the single-tone resides within the single band as defined in Sect. IV-A.

1) Pilot Signal Generation: The pilot signal is delivered by the AWG. The number of tones 80 excluding conjugate components is set to be the same as the number of the slots within the band of interest as summarized in Table II. The offset frequency f_0 and the constant distance Δf between tones are set with 100 kHz and 2 kHz, respectively. The signal length and the measurement length must be carefully chosen to have no spectral leakage in the FFT spectrum. In the following experiments, the signal length is set to 1 ms thus the FFT resolution is 1 kHz. The frequencies of the multiple tones as well as the test signals are chosen with 1 kHz resolution so as not to occur the spectral leakage. The spectrum of the pilot signal, which is directly measured at the AWG output with a real-time oscilloscope Keysight DSO-X 93304Q is illustrated in Fig. 8. In the zoomed-in view, the single-tone within the single band as defined in Sect. IV-A is clearly seen.

2) PSF Generation: The PSF is also generated by the AWG. The frequency f_p and the number of symbols M are set as given in Table II. The spectrum of the PSF, which is directly measured at the AWG output is illustrated in Fig. 9. The zoomed-in part shows a single component at 40 MHz.

3) Output of the Mixer and the LPF: The output spectrum of the mixer at node $\check{y}_i(t)$ in Fig. 6 includes the linear combinations of the input spectrum slices $Z_l(f)$ weighted with the corresponding coefficients $c_{i,-l}$ of the PSF as explained in Sect. II. The spectra at the output of the mixer and the LPF are shown in Figs. 10 and 11, respectively. The zoomed-in parts show single linear combinations of the input pilot components weighted with PSF coefficients $c_{i,-l}$.

4) Output of the ADC: A baseband part within 2 MHz of the discrete fourier transform (DFT) for the ADC output at node

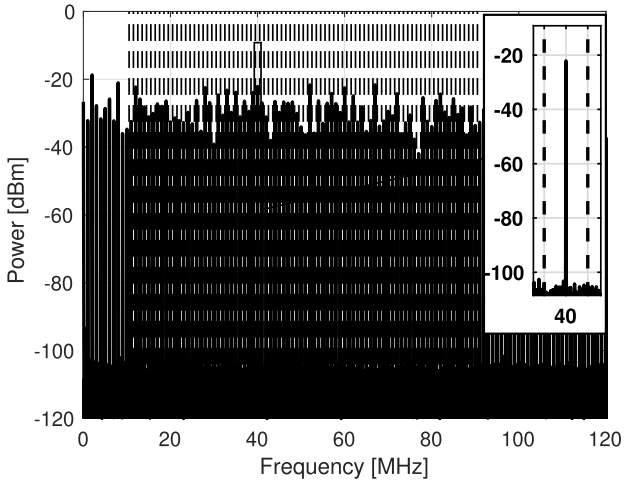

Fig. 9. Frequency-domain spectrum of the measured PSF signal. In the zoomed-in view, the single-tone resides within the single spectrum slice as shown in Fig. 3(a).

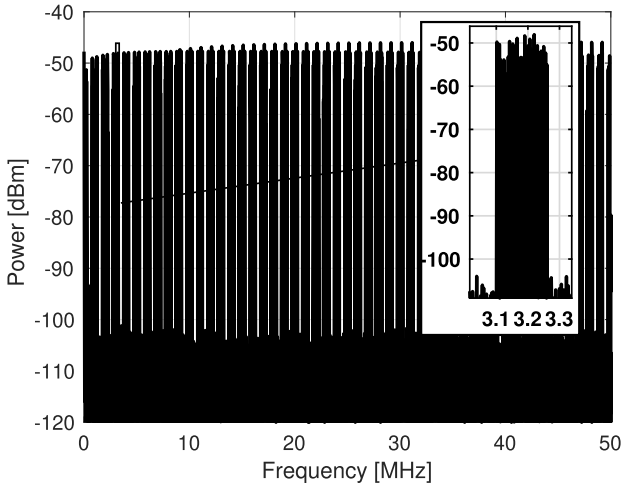

Fig. 10. Frequency-domain spectrum of the Measured mixer output signal. In the zoomed-in view, we can see a linear combinations of the input pilot components weighted with PSF coefficients $c_{i,-l}$.

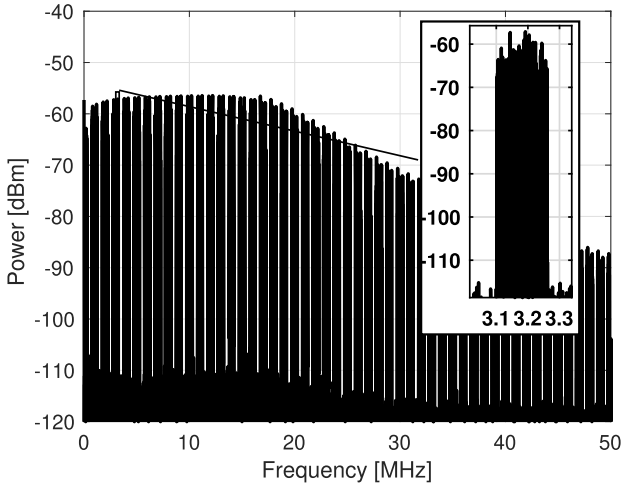

Fig. 11. Frequency-domain spectrum of the Measured LPF output signal. In the zoomed-in view, we can see a linear combinations of the input pilot components weighted with PSF coefficients $c_{i,-l}$.

$y_i(t)$ is shown in Fig. 12 that includes downconverted PSF coefficients $\tilde{c}_{i,-l}$ at f_l frequencies. At this point, the actual

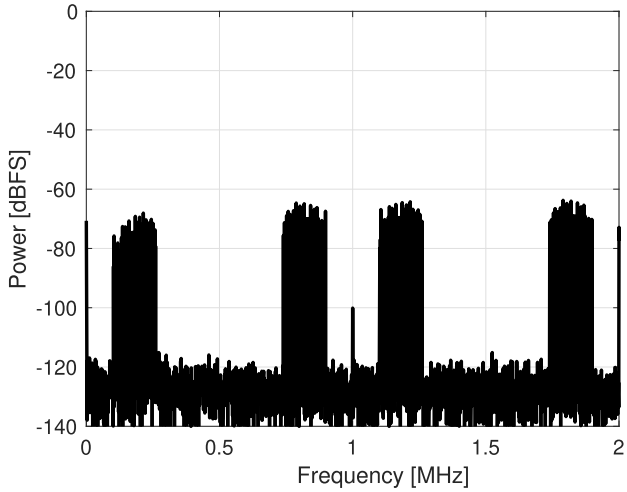

Fig. 12. A baseband part within 2 MHz of the frequency-domain spectrum for the ADC output signal with the pilot signal.

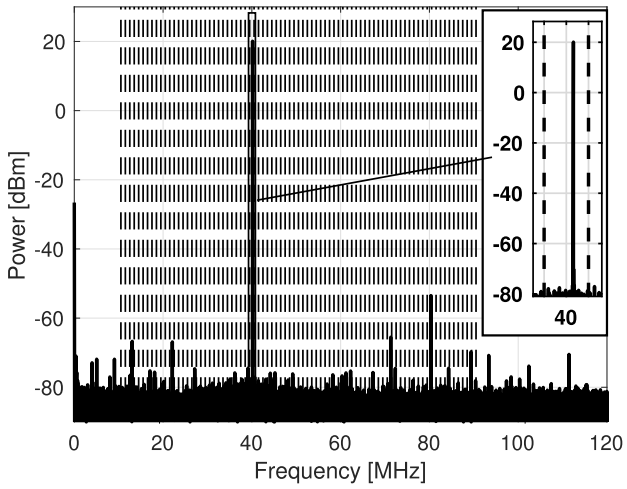

Fig. 13. Frequency-domain spectrum of the single-tone test signal with 40.16 MHz from the AWG.

sensing matrix components $\tilde{c}_{i,l}$ can be calculated based on (24).

C. Evaluation of the Calibration Performance

A single-tone signal is used as a test signal after the calibration. The reconstruction performance of the test signal with the calibrated sensing matrix is compared to that with the ideal sensing matrix in terms of NMSE and IRR to evaluate the performance of the proposed calibration method.

1) Test Signal Generation: The single-tone test signal is generated by AWG as an example spectrum with 40.16 MHz is shown in Fig. 13. According to the figure, the AWG output itself is not ideal, and some unwanted spurs are originally presented.

2) Reconstruction of the Test Signal: Firstly, the spectrum of the original test signal with 40.16 MHz directly captured by the real-time oscilloscope is shown in Fig. 14(a) and the reconstructed spectrum based on the ideal (uncalibrated) sensing matrix has shown in Fig. 14(b) whereas their time-domain waveforms have shown in Fig. 14(e) and (f), correspondingly.

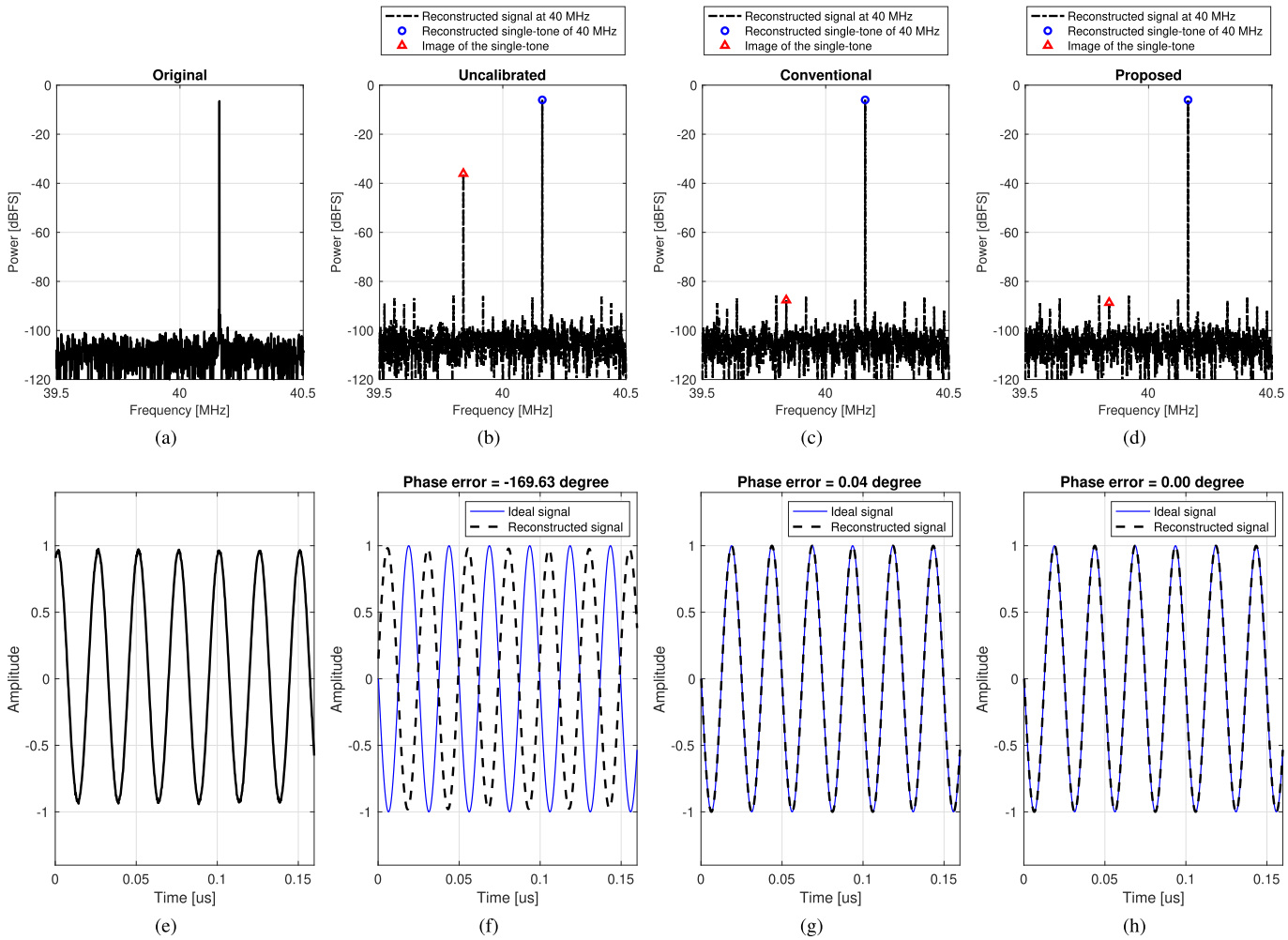

Fig. 14. Frequency-domain spectrum of (a) the input single-tone test signal with 40.16 MHz directly measured with a real-time oscilloscope, (b) the reconstructed signal based on the uncalibrated ideal A matrix, (c) that based on the calibrated A matrix constructed by the conventional method and (d) that based on the calibrated A matrix constructed by the proposed method. (e) Time-domain waveform of the first few periods of the input single-tone test signal, (f) the reconstructed single-tone test signal based on the uncalibrated ideal A matrix, (g) that based on the calibrated A matrix constructed by the conventional method and (h) that based on the calibrated A matrix constructed by the proposed method.

TABLE III
THE COMPARISON OF THE RECONSTRUCTION PERFORMANCES

Reconstruction Methods	Number of calib. meas.	40 MHz		70 MHz		Average	
		NMSE	IRR	NMSE	IRR	NMSE	IRR
Uncalibrated	N/A	5.98	30.05	5.99	30.29	5.96	37.90
Conventional	80	-61.53	81.63	-61.39	83.71	-61.11	84.15
Proposed	1	-66.01	82.67	-63.47	71.84	-62.58	76.42

The uncalibrated matrix causes large phase error in the reconstructed time-domain waveform that will result in poor NMSE performance. The highlighted circle on the spectrum shows the original single-tone test signal while the triangle depicts undesired image of the original component that is introduced by the actual sensing matrix deviated from the ideal one. The measured NMSE and IRR were 5.98 dB and 30.05 dB, respectively as summarized in Table III. The reconstructed spectrum based on the conventional method with sequential single-tone inputs is shown in Fig. 14(c) while the time-domain waveform is shown in Fig. 14(g). The conventional method needs 80 times measurements while the proposed needs only one. Furthermore, not only the number of measurements is reduced in the proposed method, but also the measurement-to-measurement timing fluctuation in the calibrated sensing matrix is fundamentally suppressed. The measured NMSE and IRR were -61.53 dB and 81.63 dB, respectively. The reconstruction based on the proposed calibration method shown in Figs. 14(d) and (h) presents the measured NMSE and the IRR of -66.01 dB and 82.67 dB, respectively. More than 50 dB NMSE and 42 dB IRR improvements are realized by the proposed calibration technique compared to the uncalibrated reconstruction. The spectra and waveforms for 70.22 MHz test signal based on the uncalibrated, conventional and proposed calibration method are shown in Fig. 15. The NMSE and the IRR for this input are also summarized in Table III. The comparison of the IRR and the NMSE performances over the band of interest is shown in Figs. 16(a) and (b), respectively. The NMSE and the IRR performances are highly dependent on the carrier frequency due to different coefficients of the PSFs. To make fair comparison, the average NMSE and the average IRR are calculated in Table III by taking average of all NMSE

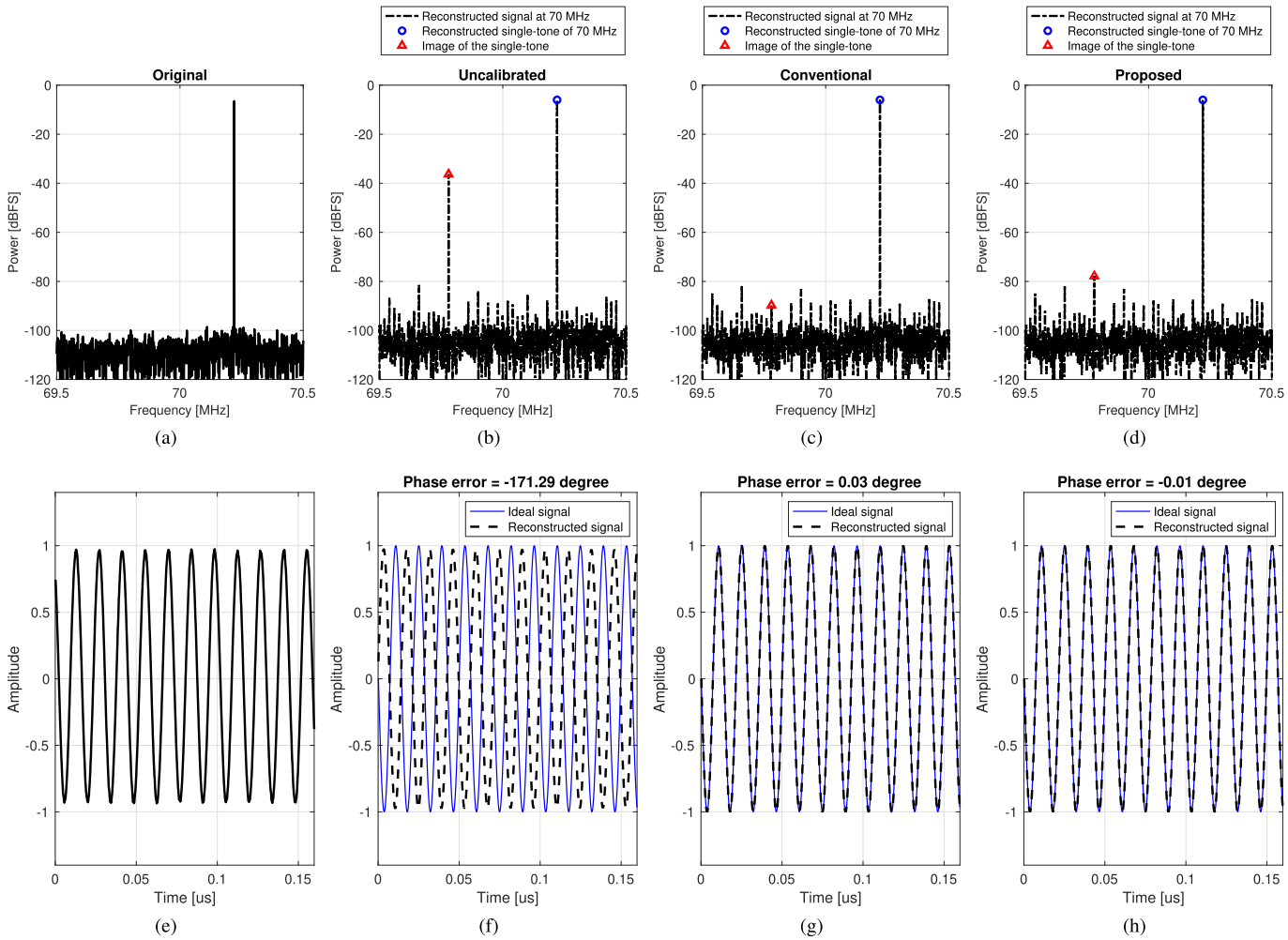

Fig. 15. Frequency-domain spectrum of (a) the input single-tone test signal with 70.22 MHz directly measured with a real-time oscilloscope, (b) the reconstructed signal based on the uncalibrated ideal A matrix, (c) that based on the calibrated A matrix constructed by the conventional method and (d) that based on the calibrated A matrix constructed by the proposed method. (e) Time-domain waveform of the first few periods of the input single-tone test signal, (f) the reconstructed single-tone test signal based on the uncalibrated ideal A matrix, (g) that based on the calibrated A matrix constructed by the conventional method and (h) that based on the calibrated A matrix constructed by the proposed method.

and IRR values for 80 carrier frequencies, correspondingly. The reconstruction based on the ideal (uncalibrated) sensing matrix has poor NMSE and IRR while the conventional and the proposed calibrations both exhibit excellent performances.

It is worth to point out that the IRR is based only on amplitude spectrum while the NMSE includes phase differences as well. The main reason that the average IRR of the proposed calibration is lower than the conventional method is that the multi-tone signal does suffer from non-linearity of the active devices. As discussed in Sect. IV-A, the tone frequencies of the pilot signal is defined as a linearly spaced frequencies. Therefore, the inter-modulated non-linear components of the linearly spaced frequencies may conflict with its main frequency set, which causes major limitation on the IRR performances. Additionally, the multi-tone signal generated from the AWG has non-linear components before injected into the MWC. This non-linearity introduces inter-modulation components around the fundamental frequencies and higher-order components into higher frequencies. Some of these components will be downconverted into the same baseband frequencies as the fundamental frequencies and they affects directly to the calibration performance. The ADC also introduces non-linearities which is another contribution to the performance degradation. For this reason, non-linearly spaced frequency set would have better performance. For example, some appropriate subset of the prime numbers can be used as the multi-tone frequencies such that the inter-modulation components of any two-tone differs from the main frequency set. To further improve the IRR performance, devices with higher linearity are recommended. At this moment, it is worth pointing out that the NMSE is more important than IRR, because the NMSE includes the phase information that is more important for the time-domain waveform reconstruction applications.

All calibrated coefficients of the sensing matrix through the proposed method do not have any phase error with other coefficients. Because all the coefficients are obtained from the single measurement while the conventional method needs $L/2 = 80$ times measurements. In the conventional method, the measurement-to-measurement timing noise is present due

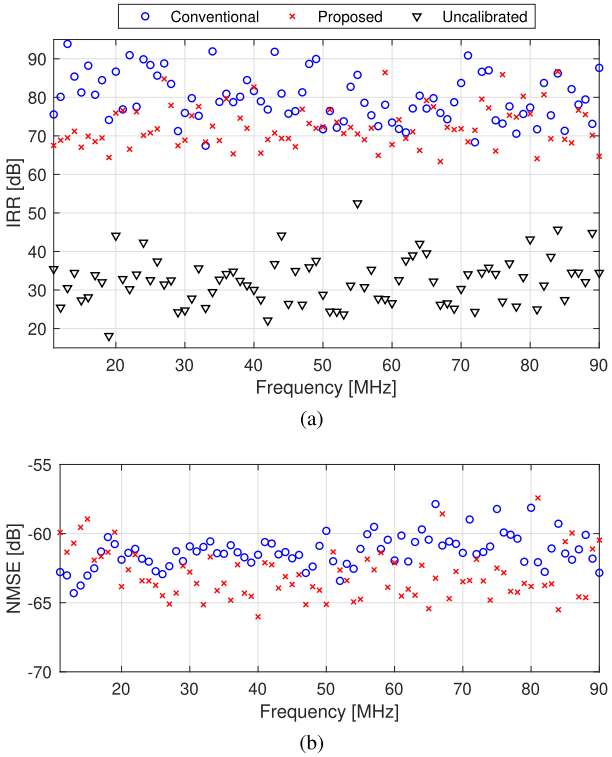

Fig. 16. The comparisons of (a) IRR and (b) NMSE performances for the frequencies over the band of interest.

to the uncertainty of the ADC sampling time and the synchronous trigger jitter of the AWG even if the calibration setup is fully synchronized. This timing noise can cause different phase deviations on the calibration of the individual coefficients. In contrast, the proposed calibration method inherently does not have the measurement-to-measurement timing noise. For that reason, the phase information is precisely acquired so that the average NMSE has enhanced more than 1 dB from the conventional calibration method as summarized in Table III. In our measurement setup, the synchronous trigger jitter of the AWG were 300 fs, which is negligibly low even for the frequencies of the single-tone calibration method. Therefore the conventional method achieves better IRR performance than the proposed. If we used a signal source with lower timing accuracy or the frequency of interest becomes higher, the IRR and the NMSE become unsatisfactory in the conventional method. In summary, the proposed method needs only single measurement to calibrate all the coefficients of the actual sensing matrix without sacrificing the reconstruction performance while the conventional method needs time-consuming $L/2$ measurements with phase errors. In addition, even after the calibration measurements, in the conventional method the subsequent digital processing takes several hours to gather all the coefficients one by one, while the proposed method does not require such computational cost.

VI. Conclusion

This paper proposed the novel calibration technique for the MWC to estimate its actual sensing matrix coefficients with only a single measurement by exploiting the dedicated non-sparse pilot signal, while the conventional calibration method repeats several measurements with single-tone inputs. For this implementation setup, the conventional calibration needs 80 measurements and the digital processing is much more complex than the proposed method. Since the proposed method requires only a single calibration measurement, it inherently does not have the measurement-to-measurement timing fluctuation that deteriorates the calibration performance in the conventional method. The calibration performance has been evaluated with NMSE and IRR, where we have achieved more than 50 dB and 42 dB improvement in NMSE and IRR, respectively.

References

[1] J. Mitola, "Software radios-survey, critical evaluation and future directions," in *Proc. Nat. Telesyst. Conf.*, 1992, pp. 13–15.
[2] S. Haykin, "Cognitive radio: Brain-empowered wireless communications," *IEEE J. Sel. Areas Commun.*, vol. 23, no. 2, pp. 201–220, Sep. 2005, doi: 10.1109/JSAC.2004.839380.
[3] K. Entesari and P. Sepidband, "Spectrum sensing: Analog (or partially analog) CMOS real-time spectrum sensing techniques," *IEEE Microw. Mag.*, vol. 20, no. 6, pp. 51–73, Jun. 2019.
[4] C. E. Shannon, "Communication in the presence of noise," *Proc. IRE*, vol. 37, no. 1, pp. 10–21, Jan. 1949.
[5] H. Nyquist, "Certain topics in telegraph transmission theory," *Trans. Amer. Inst. Electr. Eng.*, vol. 47, no. 2, pp. 617–644, Apr. 1928.
[6] M. Mishali and Y. C. Eldar, "From theory to practice: Sub-nyquist sampling of sparse wideband analog signals," *IEEE J. Sel. Topics Signal Process.*, vol. 4, no. 2, pp. 375–391, Apr. 2010.
[7] P. Wang, F. You, and S. He, "An improved signal reconstruction of modulated wideband converter using a sensing matrix built upon synchronized modulated signals," *Circuits, Syst., Signal Process.*, vol. 38, no. 7, pp. 3187–3210, Jul. 2019, doi: 10.1007/s00034-018-1009-z.
[8] W. Liu, Z. Huang, X. Wang, and W. Sun, "Design of a single channel modulated wideband converter for wideband spectrum sensing: Theory, architecture and hardware implementation," *Sensors*, vol. 17, no. 5, p. 1035, May 2017.
[9] E. Israeli *et al.*, "Hardware calibration of the modulated wideband converter," in *Proc. IEEE Global Commun. Conf.*, Dec. 2014, pp. 948–953.
[10] N. Fu, S. Jiang, L. Deng, and L. Qiao, "Successive-phase correction calibration method for modulated wideband converter system," *IET Signal Process.*, vol. 13, no. 6, pp. 624–632, Aug. 2019.
[11] P. Wang, F. You, and S. He, "Design of broadband compressed sampling receiver based on concurrent alternate random sequences," *IEEE Access*, vol. 7, pp. 135525–135538, 2019.
[12] F. You, P. Shang, and P. Wang, "Design of a low-cost integrated RF front-end for a modulated-wideband-converter based receiver," in *Proc. IEEE Asia–Pacific Microw. Conf. (APMC)*, Nov. 2017, pp. 1099–1102.
[13] M. Mishali and Y. Eldar, "Wideband spectrum sensing at sub-Nyquist rates [Applications Corner]," *IEEE Signal Process. Mag.*, vol. 28, no. 4, pp. 102–135, Jul. 2011.
[14] M. Mishali, Y. C. Eldar, O. Dounaevsky, and E. Shoshan, "Xampling: Analog to digital at sub-Nyquist rates," *IET Circuits, Devices Syst.*, vol. 5, no. 1, pp. 8–20, Jan. 2011.
[15] D. Adams, Y. Eldar, and B. Murmann, "A mixer frontend for a four-channel modulated wideband converter with 62 dB blocker rejection," in *Proc. IEEE Radio Freq. Integr. Circuits Symp. (RFIC)*, May 2016, pp. 286–289.
[16] D. Adams, Y. C. Eldar, and B. Murmann, "A mixer front end for a four-channel modulated wideband converter with 62-dB blocker rejection," *IEEE J. Solid-State Circuits*, vol. 52, no. 5, pp. 1286–1294, May 2017.
[17] Y. Zhao, Y. Hen Hu, and J. Liu, "Random triggering based sub-nyquist sampling system for sparse multiband signal," 2017, *arXiv:1703.01933*. [Online]. Available: http://arxiv.org/abs/1703.01933
[18] R. T. Yazicigil, T. Haque, M. R. Whalen, J. Yuan, J. Wright, and P. R. Kinget, "Wideband rapid interferer detector exploiting compressed sampling with a quadrature analog-to-information converter," *IEEE J. Solid-State Circuits*, vol. 50, no. 12, pp. 3047–3064, Dec. 2015.

[19] R. T. Yazicigil, T. Haque, M. Kumar, J. Yuan, J. Wright, and P. R. Kinget, "A compressed-sampling time-segmented quadrature analog-to-information converter for wideband rapid detection of up to 6 interferers with adaptive thresholding," in *Proc. IEEE Radio Freq. Integr. Circuits Symp. (RFIC)*, May 2016, pp. 282–285.
[20] T. Haque, R. T. Yazicigil, K. J.-L. Pan, J. Wright, and P. R. Kinget, "Theory and design of a quadrature analog-to-information converter for energy-efficient wideband spectrum sensing," *IEEE Trans. Circuits Syst. I, Reg. Papers*, vol. 62, no. 2, pp. 527–535, Feb. 2015.
[21] J. Park, J. Jang, and H.-N. Lee, "A calibration for the modulated wideband converter using sinusoids with unknown phases," in *Proc. 9th Int. Conf. Ubiquitous Future Netw. (ICUFN)*, Jul. 2017, pp. 951–955.
[22] L. Chen, J. Jin, and Y. Gu, "A calibration system and perturbation analysis for the modulated wideband converter," in *Proc. IEEE 10th Int. Conf. SIGNAL Process. Proc.*, Oct. 2010, pp. 78–81.
[23] Y. K. Alp, A. B. Korucu, A. T. Karabacak, A. C. Gurbuz, and O. Arikan, "Online calibration of modulated wideband converter," in *Proc. 24th Signal Process. Commun. Appl. Conf. (SIU)*, May 2016, pp. 913–916.
[24] M. Mishali and Y. C. Eldar, "Blind multiband signal reconstruction: Compressed sensing for analog signals," *IEEE Trans. Signal Process.*, vol. 57, no. 3, pp. 993–1009, Mar. 2009.
[25] Z. Byambadorj, K. Asami, T. J. Yamaguchi, A. Higo, M. Fujita, and T. Iizuka, "Theoretical analysis of noise figure for modulated wideband converter," *IEEE Trans. Circuits Syst. I, Reg. Papers*, vol. 67, no. 1, pp. 298–308, Jan. 2020.
[26] Y. C. Pati, R. Rezaiifar, and P. S. Krishnaprasad, "Orthogonal matching pursuit: Recursive function approximation with applications to wavelet decomposition," in *Proc. 27th Asilomar Conf. Signals, Syst. Comput.*, Nov. 1993, pp. 40–44.
[27] P. Welch, "The use of fast Fourier transform for the estimation of power spectra: A method based on time averaging over short, modified periodograms," *IEEE Trans. Audio Electroacoustics*, vol. 15, no. 2, pp. 70–73, Jun. 1967.
[28] S. Boyd, "Multitone signals with low crest factor," *IEEE Trans. Circuits Syst.*, vol. 33, no. 10, pp. 1018–1022, Oct. 1986.
[29] N. Dong and J. Wang, "Channel gain mismatch and time delay calibration for modulated wideband converter-based compressive sampling," *IET Signal Process.*, vol. 8, no. 2, pp. 211–219, Apr. 2014.
[30] *Datasheet ADL5801*. Accessed: Feb. 9, 2020. [Online]. Available: https://www.analog.com/en/products/adl5801.html#product-overview
[31] *Datasheet LTC6604*. Accessed: Feb. 9, 2020. [Online]. Available: https://www.analog.com/media/en/dsp-documentation/evaluation-kit-manuals/dc1418A.pdf
[32] *Datasheet LTC2207*. Accessed: Feb. 9, 2020. [Online]. Available: https://www.analog.com/media/en/technical-documentation/data-sheets/22076fc.pdf

Zolboo Byambadorj (Graduate Student Member, IEEE) received the B.S. and M.S. degrees in communication engineering from the National University of Mongolia, Ulaanbaatar, Mongolia, in 2008 and 2012, respectively. He is currently pursuing the Ph.D. degree in electrical engineering with The University of Tokyo, Tokyo, Japan. In 2008, he joined the Department of Electrical and Communication Engineering, National University of Mongolia, as a Faculty Member. His current research interests include wireless communication systems and sub-Nyquist sampling systems.

Koji Asami (Member, IEEE) received the master's degree in electronic engineering and the Ph.D. degree in electronics and information engineering from Gunma University, Japan, in 1991 and 2009, respectively.

In 1991, he joined the Gunma Research and Development Center, Advantest Corporation, where he dedicated his time to researching signal processing techniques for mixed-signal and RF LSI test, including the digital modulation analysis. He has also been a Visiting Professor with the Graduate School of Science and Technology, Gunma University, since 2015, and a Researcher with the Advantest D2T Research Division, VDEC, The University of Tokyo, since 2017. Since 2019, he has been researching measurement methodologies for wireless communication devices with Advantest Laboratories Ltd. His research interests include signal processing algorithm for testing RF and analog devices and improving the automatic test equipment (ATE) performance.

Takahiro J. Yamaguchi (Member, IEEE) received the B.S. degree in applied physics from Fukui University, Fukui, Japan, in 1976, and the M.S. degree in physics and the Ph.D. degree in electronic engineering from Tohoku University, Sendai, Japan, in 1978, and 1999, respectively.

In 1978, he joined Advantest Corporation, where he was a Research and Development Project Manager for Fourier analyzers, FFT-based servo analyzers, Michelson-type optical spectrum analyzers, and TV signal analyzers. Until 2017, he was with Advantest Laboratories Ltd., Sendai. From 2009 to 2014, he was a Visiting Professor with Gunma University, Japan. From 2009 to 2017, he was a Researcher with VDEC, The University of Tokyo, where he is currently a Project Academic Support Staff. He and his group have presented 14 articles at ITC since 2000, 11 articles at ISSCC, VLSI CIRCUITS, CICC, RFIC, A-SSCC, and ISCAS, and seven journal articles. From 2010 to 2015, he has served as a member of the Technical Program Committee of the IEEE Custom Integrated Circuits Conference (CICC). He was a co-recipient of the DesignCon2007 Best Paper and the Honorable Mention Award at ITC2010 for ITC2009 Jitter Separation Paper.

Akio Higo (Member, IEEE) received the B.E. degree from Seikei University, Tokyo, Japan, in 2002, and the M.E. and Ph.D. degrees from the Department of Electrical Engineering, The University of Tokyo, Tokyo, in 2004 and 2007, respectively.

From 2007 to 2012, he was an Assistant Professor with the Research Center for Advanced Science and Technology. From 2012 to 2016, he was an Assistant Professor with the World Premier Initiative Advanced Institute for Materials Research, Tohoku University, Sendai, Japan. Since 2017, he has been a Project Lecturer with the D2T Research Division, VLSI Design and Education Center, The University of Tokyo. His research interests are in NEMS/MEMS, nanolithography for III–V materials and silicon, and silicon photonics.

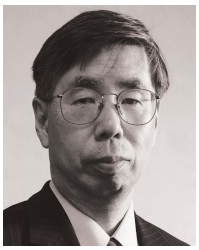

Masahiro Fujita (Member, IEEE) received the Ph.D. degree in information engineering from The University of Tokyo in 1985, with a focus on model checking of hardware designs by using logic programming languages.

In 1985, he joined Fujitsu as a Researcher and started to work on hardware automatic synthesis as well as formal verification methods and tools, including enhancements of BDD-/SAT-based techniques. From 1993 to 2000, he was the Director of the Fujitsu Laboratories of America and headed a hardware formal verification group developing a formal verifier for real-life designs having more than several million gates. The developed tool has been used in production internally at Fujitsu and externally as well. Since March 2000, he has been a Professor with the VLSI Design and Education Center, The University of Tokyo. He has done innovative work in the areas of hardware verification, synthesis, testing, and software verification—mostly targeting embedded software and web-based programs. He has been involved in a Japanese governmental research project for dependable system designs and has developed a formal verifier for C programs that could be used for both hardware and embedded software designs. The tool is now under evaluation jointly with industry under governmental support. He has authored or coauthored ten books and has more than 200 publications. His current research interests include synthesis and verification in system on chip (SoC), hardware/software co-designs targeting embedded systems, digital/analog co-designs, and formal analysis, verification, and synthesis of web-based programs and embedded programs. He has been involved as a Program and Steering Committee Member in many prestigious conferences on CAD, VLSI designs, software engineering, and so on.

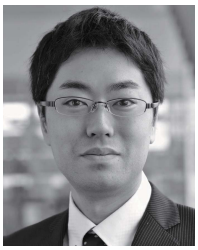

Tetsuya Iizuka (Senior Member, IEEE) received the B.S., M.S., and Ph.D. degrees in electronic engineering from The University of Tokyo, Tokyo, Japan, in 2002, 2004, and 2007, respectively.

From 2007 to 2009, he was with THine Electronics Inc., Tokyo, Japan, as a high-speed serial interface circuit Engineer. He joined The University of Tokyo in 2009, where he is currently an Associate Professor with Systems Design Laboratory, School of Engineering. From 2013 to 2015, he was a Visiting Scholar with the University of California, Los Angeles, CA, USA. His current research interests include data conversion techniques, high-speed analog integrated circuits, digitally assisted analog circuits, and VLSI computer-aided design.

Dr. Iizuka is a member of the Institute of Electronics, Information and Communication Engineers (IEICE). He was a member of the IEEE International Solid-State Circuits Conference (ISSCC) Technical Program Committee from 2013 to 2017 and a member of the IEEE Custom Integrated Circuits Conference (CICC) Technical Program Committee from 2014 to 2019. From 2016 to 2018, he served as the Editor of *IEICE Electronics Express* (ELEX). He is currently serving as a member of the IEEE Asian Solid-State Circuits Conference (A-SSCC) Technical Program Committee. He was a recipient of the Young Researchers Award from IEICE in 2002, the IEEE International Conference on Electronics, Circuits and Systems Best Student Paper Award in 2006, the Yamashita SIG Research Award from the Information Processing Society, Japan in 2007, the 21st Marubun Research Encouragement Commendation from Marubun Research Promotion Foundation in 2018, the 13th Wakashachi Encouragement Award First Prize in 2019, and the 18th Funai Academic Prize from Funai Foundation for Information Technology in 2019. He was a co-recipient of the IEEE International Test Conference Ned Kornfield Best Paper Award in 2016.